

Evaluation of Impacts of Driving Forces on Neoclassical Transport with Weight-Splitting Method

Keiji FUJITA¹⁾ and Shinsuke SATAKE^{1,2)}

¹⁾The Graduate University for Advanced Studies (SOKENDAI), 322-6 Oroshi-cho, Toki 509-5292, Japan

²⁾National Institute for Fusion Science, 322-6 Oroshi-cho, Toki 509-5292, Japan

(Received 7 October 2021 / Accepted 11 April 2022)

Neoclassical transport is caused by the non-equilibrium distribution function produced by the driving forces due to quasi-steady but non-uniform plasma state parameters and electromagnetic fields as well as by the Coulomb interactions. In this article, we present a method to evaluate the impact of each driving force on neoclassical transport by a single global drift-kinetic simulation. This method can be used to evaluate the impacts of each driving force not only in one-dimensional forms as transport coefficients, but also in multidimensional forms as how the impacts of each driving force are distributed over the phase space. As an application of the method, we investigate the impacts of each driving force on particle density variations in an impurity hole plasma and demonstrate that the impact of the outward driving force of the temperature gradient on the radial impurity flux becomes as large as the impact of the inward driving force of the negative ambipolar radial electric field. Further, we show that the variation of electrostatic potential on each flux surface, Φ_1 , which is involved in several factors in a drift-kinetic equation, affects the density variations specifically through the radial $E \times B$ drift.

© 2022 The Japan Society of Plasma Science and Nuclear Fusion Research

Keywords: neoclassical transport, plasma confinement

DOI: 10.1585/pfr.17.1403065

1. Introduction

The aim of neoclassical transport studies is to understand the transport of particles and energy in a plasma caused by the steady but inhomogeneous plasma profiles and electromagnetic fields and by the Coulomb interactions between the charged particles. From the microscopic point of view, the transport is caused by the deviation of the distribution function from the local thermodynamic equilibrium distribution,

$$\delta f_a \equiv f_a - f_{aM}, \quad (1)$$

where f_a is the total 1-particle distribution function and f_{aM} is the local Maxwellian,

$$f_{aM}(r, v) = n_a(r) \left(\frac{m_a}{2\pi T_a(r)} \right)^{3/2} \exp\left(-\frac{m_a v^2}{2T_a(r)}\right), \quad (2)$$

which represents the local equilibrium distribution, where n_a denotes the density, T_a the temperature, m_a the mass, v the magnitude of the velocity \mathbf{v} , and r the radial coordinate, respectively. The subscript a is the species label. In (1), it is assumed that

$$\delta f_a / f_{aM} \sim \delta \ll 1, \quad (3)$$

where $\delta = \rho/L$, ρ is the thermal gyroradius, and L is the typical length scale of the plasma. The macroscopic fluxes are evaluated with the distribution function by

$$J_{ai} = \left\langle \int d^3v j_{ai} \delta f_a \right\rangle, \quad (4)$$

where J_{ai} is the i -th flux and j_{ai} is the corresponding microscopic flow, such as $\mathbf{v}_d \cdot \nabla r$ for the radial particle flux, where \mathbf{v}_d is the drift velocity, and $\langle \dots \rangle$ denotes the flux surface average.

The macroscopic fluxes are flux-surface-averaged quantities and have little information on the causes of them. On the other hand, the transport coefficients D_{ij}^{ab} relate the fluxes to driving forces linearly as

$$J_{ai} = \sum_b \sum_j D_{ij}^{ab} X_{bj}, \quad (5)$$

under the assumptions that the system is close to equilibrium and the driving forces are small enough to neglect the higher-order nonlinear terms. Throughout this article, we will assume that $X_{aj} \sim 1/L$ for all j and a . The transport coefficients thus provide the information on how much each driving force contributes to the flux-surface-averaged fluxes.

One approach to evaluating the contribution of a specific driving force is setting all other driving forces to zero. This can be a practical option for local simulation because the radially local approximation enables us to set the gradients of the background parameters to arbitrary values, including zero, on a specific flux surface keeping the local values of the background parameters themselves. However, this is not a realistic option for global simulation. The first reason is simply the numerical cost. Since the calculation time required for a global simulation is tens or hundreds of times larger than those of local simulations

author's e-mail: fujita.keiji@nifs.ac.jp

for a single case. It is thus not always possible to investigate the impact of each driving force by this method one by one, especially when several species are present in the plasma. The second reason, which is more crucial, is the global effects. The outputs of global simulation depend on the global structure of the background parameter profiles. A self-consistent calculation of the ambipolar E_r requires all the driving forces to be considered as well. We thus cannot modify the profiles of the background parameters in an arbitrary manner. Therefore, we have developed a new method to evaluate the impacts of each driving force by a single δf simulation without a significant increase in the numerical cost. This method can be implemented in local codes as well as global codes.

In this article, we present how to implement and apply the method to evaluate the impacts of driving forces on particle density variations. Here, we focus on density variations instead of the transport coefficients because the transport coefficients are also flux-surface-averaged, one-dimensional quantities. A lot of information carried by the distribution function is lost in the averaging process. The information lost in the process is potentially very valuable for the transport study since the transport is caused by the characteristic orbits of the particles and the inhomogeneous distribution of the particles over the phase space.

Recently, it has been discussed that several effects that have conventionally been neglected can be important for determining neoclassical impurity transport. The first example is the variation of electrostatic potential on each flux surface $\Phi_1 \equiv \Phi - \Phi_0$, where Φ is the total electrostatic potential and $\Phi_0 = \Phi_0(r)$ is the flux-function part of it. The potential variation Φ_1 is produced mainly by the bulk ion density variation, and how Φ_1 couples with the impurity density variations has been a subject of interest (e.g.[1–5]). The second is the effects of external heating such as neutral beam injection (NBI) [6] that can also give rise to asymmetry in density profiles on flux surfaces [7, 8]. The third is synergy effects between neoclassical and turbulent transport. Impurity transport can be affected by the synergy through the density perturbation [9]. Measurement of impurity density variations is of interest to experimental studies as well [10]. Thus, implementing a method that can evaluate the density variations with respect to each driving factor, including those yet to be investigated, is important to investigate the detailed mechanism behind impurity transport.

The rest of this article is organized as follows. In Sec. 2, we present the theoretical consideration underlying the method. In Sec. 3, we show how to implement the method in Monte-Carlo δf simulation codes. Then, an application of the method is presented in Sec. 4. Finally, further potential applications of the method are discussed, and the study is concluded in Sec. 5.

2. Linearized Drift-Kinetic Equation

For generality, we consider the formulation including Φ_1 . To consider the impact of Φ_1 , it is convenient to choose the lowest order distribution function as

$$f_{a0} = f_{aM} \exp(-Z_a e \Phi_1 / T_a). \quad (6)$$

Then, the non-adiabatic perturbation of the distribution function, δf_a , is determined by a drift-kinetic equation:

$$\frac{d\delta f_a}{dt} = -\frac{df_{a0}}{dt} + C(f_a), \quad (7)$$

where C and d/dt represent the collision operator and the total time derivative along a guiding-center drift orbit, respectively. Under the assumption (3), the collision operator can be linearized as $C(f_a) \simeq C_a^L(\delta f_a) \equiv \sum_b C_{ab}^L(\delta f_a) \equiv \sum_b [C_{ab}^T(\delta f_a) + C_{ab}^F(\delta f_b)]$, where C_{ab}^T and C_{ab}^F are test-particle and field-particle parts of the collision operator, respectively. Up to the first order of δ , the right-hand side of (7) can also be expanded as

$$\frac{df_{a0}}{dt} = \mathbf{v}_d \cdot \nabla r f_{a0} \left[X_{a1} + \left(x_a^2 + \frac{Z_a e \Phi_1}{T_a} - \frac{3}{2} \right) X_{a2} \right], \quad (8)$$

$$\equiv f_{a0} (j_{a1} X_{a1} + j_{a2} X_{a2}), \quad (9)$$

with the driving forces,

$$X_{a1} = \frac{n'_a}{n_a} - \frac{Z_a e E_r}{T_a}, \quad (10)$$

$$X_{a2} = \frac{T'_a}{T_a}, \quad (11)$$

and the microscopic flows,

$$j_{a1} = \mathbf{v}_d \cdot \nabla r, \quad (12)$$

$$j_{a2} = \mathbf{v}_d \cdot \nabla r \left(x_a^2 + \frac{Z_a e \Phi_1}{T_a} - \frac{3}{2} \right), \quad (13)$$

where $Z_a e$ is the charge of the species a , $E_r = -d\Phi_0/dr$ is the radial electric field, $x_a^2 = m_a v^2 / (2T_a)$, and the prime denotes the radial derivative. The radial drift velocity $\mathbf{v}_d \cdot \nabla r$ consists of the radial components of the magnetic drift \mathbf{v}_m and the $E \times B$ drift \mathbf{v}_E as $\mathbf{v}_d \cdot \nabla r = (\mathbf{v}_m + \mathbf{v}_E) \cdot \nabla r$. The radial $E \times B$ drift is generated by Φ_1 :

$$\mathbf{v}_E \cdot \nabla r = \mathbf{v}_{E1} \cdot \nabla r \equiv \frac{\mathbf{B} \times \nabla \Phi_1}{B^2} \cdot \nabla r. \quad (14)$$

Therefore, Φ_1 is involved in three different factors in (9): the $E \times B$ drift in \mathbf{v}_d , the potential energy carried by j_{a2} , and the adiabatic response in f_{a0} . For moderate Z_a , $Z_a e \Phi_1 / T_a \sim O(\delta)$. Thus, in each of these forms, the impact of Φ_1 is usually smaller than the conventional terms by δ :

$$\frac{Z_a e \Phi_1}{T_a x_a^2} \sim \frac{Z_a e \Phi_1}{m_a v^2} \sim \frac{\mathbf{v}_{E1}}{\mathbf{v}_m} \sim \delta. \quad (15)$$

Note that Φ_1 is produced by the density variations [1, 4]:

$$\Phi_1 = \frac{1}{e} \left(\sum_I \frac{Z_I^2 n_{I0}}{T_i} + \frac{n_{e0}}{T_e} \right)^{-1} \sum_a Z_a \int d^3v \delta f_a, \quad (16)$$

where the subscript I refers to ion species, and all the ion species are assumed to have the same temperature T_i . Thus, δf_a enters (9), and therefore in the right-hand side of the drift-kinetic Eq. (7). However, we can still assume that (9) is approximately independent of δf_a . For impurity ions, it is because Φ_1 is mainly determined by the density variation of the bulk ions, i.e.,

$$\Phi_1 \simeq \frac{Z_i}{e} \left(\sum_I \frac{Z_I^2 n_{I0}}{T_i} + \frac{n_{e0}}{T_e} \right)^{-1} \int d^3v \delta f_i, \quad (17)$$

if the concentration of the impurity ions is small. In (17), the electron density variation is also neglected because the electron response can be assumed to be adiabatic: $\delta f_e = 0$. In the present study, the low concentration of the impurity ions is a natural consequence of the input profiles, and the adiabatic response is assumed in evaluating Φ_1 by neglecting δn_e . For the bulk ions, on the other hand, the impact of Φ_1 is small because of the smallness of $Z_a = Z_i$ in (15) and the formulation without Φ_1 can be assumed for the qualitative analysis. Then, each factors in (9) are reduced as

$$\begin{aligned} f_{a0} &\rightarrow f_{aM}, \\ \mathbf{v}_d \cdot \nabla r &\rightarrow \mathbf{v}_m \cdot \nabla r, \\ j_{a2} &\rightarrow \mathbf{v}_m \cdot \nabla r \left(X_a^2 - \frac{3}{2} \right). \end{aligned} \quad (18)$$

Under these considerations, we obtain a linearized drift-kinetic equation

$$\frac{d\delta f_a}{dt} = -f_{a0} (j_{a1} X_{a1} + j_{a2} X_{a2}) + C_a^L(\delta f_a). \quad (19)$$

Then, corresponding to each driving force, the distribution function can be decomposed as

$$\delta f = \sum_b \sum_{j=1}^2 \delta f_{ab}^j, \quad (20)$$

where δf_{ab}^j is proportional to X_{bj} and each component satisfies either of the decomposed drift-kinetic equations

$$\frac{d}{dt} \delta f_{aa}^j = -j_{aj} f_{a0} X_{aj} + C_a^L(\delta f_{aa}^j), \quad (21)$$

$$\frac{d}{dt} \delta f_{ab}^j = C_a^L(\delta f_{ab}^j), \quad (a \neq b). \quad (22)$$

Thus, for example, the integral

$$\delta n_{aj} = \int d^3v \delta f_{aa}^j \quad (23)$$

gives the density variation caused by the i -th driving force regardless of the other driving forces. Note here that the

collision terms do not contribute to the density variation in the form of (23) since the linearized Coulomb collision operator does not affect the spatial variables (or equivalently by the particle conservation law, $0 = \int dt \int d^3v C^L(\delta f)$). The collisions affect the density variation through the velocity variables in (12) and (13) instead.

3. Weight-Splitting Method

In this section, we explain how to implement the scheme described above in Monte-Carlo two-weight δf simulation codes. In the two-weight δf scheme [11, 12], the distribution functions are represented by the products of the marker particle distribution $g_a(\mathbf{Z}, t)$ and the weight fields $P_a(\mathbf{Z}, t)$ and $W_a(\mathbf{Z}, t)$, respectively, as

$$f_{a0}(\mathbf{Z}, t) = P_a(\mathbf{Z}, t) g_a(\mathbf{Z}, t), \quad (24)$$

$$\delta f_a(\mathbf{Z}, t) = W_a(\mathbf{Z}, t) g_a(\mathbf{Z}, t), \quad (25)$$

where \mathbf{Z} denotes the guiding-center phase variables, and f_{a0} is a Maxwellian if $\Phi_1 = 0$ otherwise $f_{a0} = f_{aM} \exp(-Z_a e \Phi_1 / T_a)$. Each marker particle is assigned two weights $w_{a,i}$ and $p_{a,i}$ that are defined as the values of the weight fields W_a and P_a at the particle position in the phase space, \mathbf{Z}_i , respectively:

$$w_{a,i}(t) = W_a(\mathbf{Z}_i(t), t), \quad (26)$$

$$p_{a,i}(t) = P_a(\mathbf{Z}_i(t), t), \quad (27)$$

where i is the marker particle label.

In Monte-Carlo δf codes, the test-particle part of the linearized collision operator, $C_a^T = \sum_b C_{ab}^T$, is described by a diffusion process in the velocity space [13, 14]. The weight $w_{a,i}$ is then determined by solving the equation

$$\frac{Dw_{a,i}}{Dt} = -p_{a,i} (j_{a1} X_{a1} + j_{a2} X_{a2}) + \mathcal{P}_a, \quad (28)$$

where $D/Dt \equiv d/dt - C_a^T$ and \mathcal{P}_a represents the field-particle operator. Then, corresponding to (20), we can split the weight as

$$w_{a,i} = \sum_b \sum_{j=1}^2 w_{ab,i}^j, \quad (29)$$

where each component is a solution of either of the equations corresponding to (22),

$$\frac{D}{Dt} w_{aa,i}^j = -p_{a,i} j_j X_{aj} + \mathcal{P}_a,$$

$$\frac{D}{Dt} w_{ab,i}^j = \mathcal{P}_a, \quad (a \neq b). \quad (30)$$

Evaluating the solutions of (30), instead of (28), gives the δf components with respect to each driving force. See [4] for how to construct multi-dimensional continuous profiles of averaged quantities, such as δn_a , from $w_{a,i}$.

4. Application of the Method

4.1 Impurity hole plasma

In our previous study, we investigated the impurity transport in an impurity hole plasma [5]. An impurity hole observed in the Large Helical Device (LHD) is a hollow impurity density profile formed in the core plasma where an inward-pointing E_r exists [15, 16]. The formation of an impurity hole contradicts the prediction of conventional neoclassical theory. Under such a condition, inward fluxes of moderate- Z to high- Z impurities are anticipated by the conventional neoclassical theory since the driving force due to the E_r (the second term in (10)) is proportional to the charge $Z_a e$. The neoclassical simulations with radially local codes have confirmed this prediction as well [2, 3].

For this reason, turbulent transport is suspected to play a key role behind the phenomenon, but to date, no satisfactory explanation has been provided by turbulent transport studies [17, 18]. On the other hand, through the investigation of the phenomenon, studies showed that an outward driving force of the large temperature gradient can compete with or possibly overcome the inward E_r driving force [3, 19]. The studies suggested that producing the outward impurity fluxes by neoclassical simulation may remain possible if some more elaborate model is used. We thus performed numerical simulations using a radially global neoclassical code FORTEC-3D, which is built on the Monte-Carlo two weight δf schemes [14, 20, 21]. As a result, although some issues remain unsolved, we successfully reproduced the outward impurity fluxes, and it was in fact indicated that the ion temperature gradient ∇T_i and the ambipolar E_r contribute to the flux in the same level, each in the opposite direction [5]. It was also confirmed that Φ_1 can contribute to driving the impurity flux further outwardly. However, the contributions of each driving force to the macroscopic fluxes have not been quantitatively estimated, since in particle codes such as FORTEC-3D, the fluxes are usually evaluated by integrals (4), not by the combination of the driving forces as (5). We thus apply the new method described above to make a quantitative evaluation of the impact of each driving force on the impurity transport and to examine in which way Φ_1 mainly contributes to the flux enhancement.

4.2 Simulation setup and the results

The simulation setup and the input plasma profiles are the same as Case A in [5]. We apply the method to the cases with and without Φ_1 . A standard LHD configuration with a major radius of $R_0 = 3.7$ m and a minor radius of $a = 0.62$ m is assumed. The plasma contains three ion species: hydrogen H^{1+} , helium He^{2+} , and carbon C^{6+} . Carbon is the most typical ion species that has been observed to form an impurity hole. The n - T profiles are shown in Fig. 1. The hollow region of the carbon density profile ($0.1 < r/a < 0.6$) corresponds to an impurity hole. All the ion species are assumed to have the same temperature T_i .

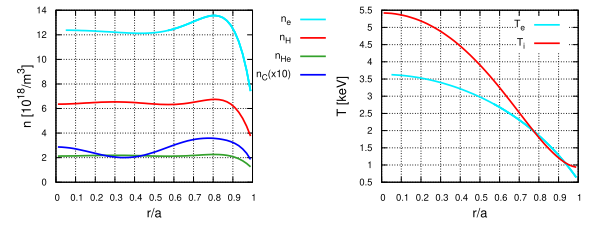


Fig. 1 Density profiles (left) and the temperature profiles (right). All the ion species are assumed to be in thermal equilibrium with each other.

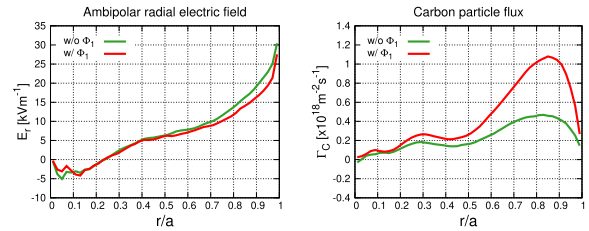


Fig. 2 Input profiles of the ambipolar E_r (left) and the resulting Γ_C (right). The green and red lines represent the results with and without Φ_1 , respectively.

A difference in the simulation setup from the previous study is that the profiles of E_r are fixed during the evaluation of δn_C so that all X_j are constant on each flux surface. After about 10 carbon collision time ($\sim 10\tau_C$), E_r and the radial particle fluxes Γ_a of all species reach steady values. We then use the steady E_r profiles as the input values and continue the simulation for about another carbon collision time ($\sim \tau_C$) to evaluate the carbon density variation δn_C . Thus, the additional numerical cost for applying the method is about 10% of the original simulation. The time evolution of Φ_1 is not stopped for the case with Φ_1 , but after the system reaches a quasi-steady state, Φ_1 does not show appreciable changes. The input profiles of the ambipolar E_r and the resulting radial carbon particle flux for the present cases are shown in Fig. 2.

4.3 Case without Φ_1

We first represent the result of the case without Φ_1 . Figure 3 represents the carbon density variation, δn_C , on three different flux surfaces: from left to right, $r/a = 0.2, 0.25$, and 0.3 , respectively. These surfaces belong in the region where E_r changes its sign from negative to positive. The horizontal and vertical axes correspond to the toroidal angle (ζ) and the poloidal angle (θ) in Boozer coordinates, respectively. The upper figures are the results evaluated with the unsplit weight, w_C , and the lower figures with the sum of the split weights, $\sum_j w_{CC}^j$. The smallness of the difference between the upper and lower figures justifies the linear expansion of δf in the driving forces (20).

Since $\mathbf{v}_d \cdot \nabla r \sim -\sin \theta$, the radial particle flux is effectively produced by the $\sin \theta$ component of δn_a . The

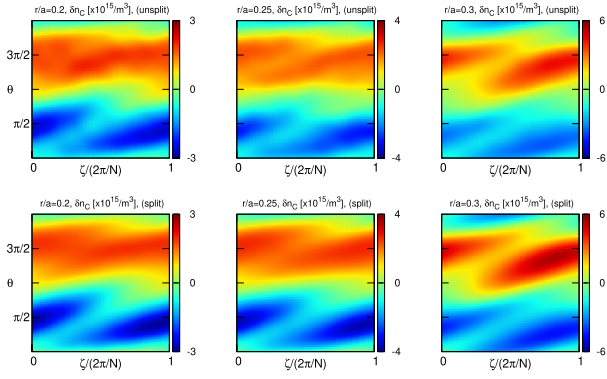


Fig. 3 Carbon density variation profile on the flux surface at $r/a = 0.2$ (left), $r/a = 0.25$ (center), and $r/a = 0.3$ (right) for the case without Φ_1 . The upper figures correspond to the result evaluated with unsplit weights and the lower figures to the sum of the split weights. N is the toroidal symmetry number ($N = 10$ for LHD).

positive $\sin \theta$ component corresponds to an up-down (top-bottom) asymmetric distribution of the particles: the density is high at the top ($\theta = \pi/2$) and low at the bottom ($\theta = 3\pi/2$) regions, respectively, and which leads to an inward particle flux. Conversely, the negative $\sin \theta$ component contributes to an outward flux. In light of this consideration, we see that the phase structures of the carbon density profiles indicate that the flux is driven outwardly, as indeed shown in Fig. 2.

Now, let us look into the contribution of each driving force to the carbon density variation δn_C . In order to compare the impacts of E_r and ∇T_C on δn_C directly, we decompose X_{C1} as $X_{C1} = X_{\nabla n} + X_E$, where

$$X_{\nabla n} \equiv \frac{n'_C}{n_C}, \quad X_E \equiv -\frac{Z_C e E_r}{T_C}, \quad (31)$$

and evaluate the density variation with respect to $X_{\nabla n}$, X_E , and $X_{\nabla T} \equiv X_{C2} = T'_C/T_C$, respectively.

Figure 4 represents the carbon density variation due to $X_{\nabla n}$ (top), X_E (center), and $X_{\nabla T}$ (bottom) respectively. As in Fig. 2, from left to right, each column corresponds to $r/a = 0.2, 0.25$, and 0.3 . At $r/a = 0.2$, where $E_r < 0$, the X_E -driven component clearly contributes to the inward flux. However, the $X_{\nabla T}$ -driven part has the opposite sign, while the amplitude is almost the same as X_E -driven one. This indicates that in the impurity hole plasma, the inward impurity flux due to the negative E_r can be canceled by the outward flux due to the temperature gradient, as estimated with local simulation results in [3, 19]. This result is consistent with experimental reports that impurity holes are usually observed in the core of NBI-heated discharges where ∇T_i becomes large [10]. At $r/a = 0.25$, where $E_r \sim 0$, the amplitude of X_E -driven part decreases as it should. At $r/a = 0.3$, where $E_r > 0$, the profile of the X_E -driven part changes its sign from that of $r/a = 0.2$.

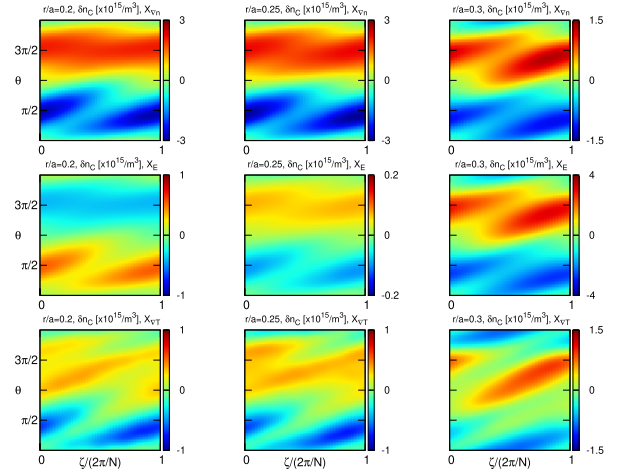


Fig. 4 Carbon density variation due to $X_{\nabla n}$ (top), X_E (center), and $X_{\nabla T}$ (bottom) for the case without Φ_1 . From left to right, each column corresponds to the flux surface at $r/a = 0.2, r/a = 0.25$, and $r/a = 0.3$, respectively. N is the toroidal symmetry number ($N = 10$ for LHD). Note that the color contour range is different for each plot.

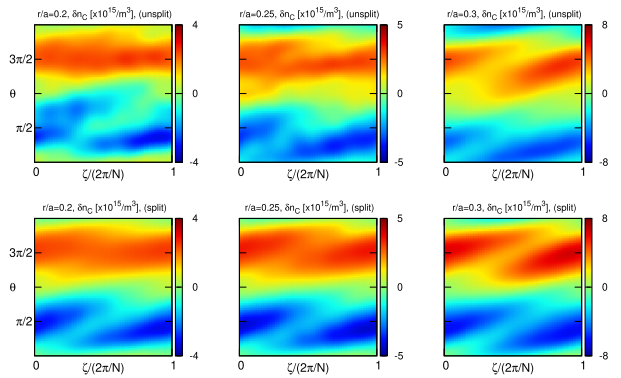


Fig. 5 Carbon density variation profile on the flux surface at $r/a = 0.2$ (left), $r/a = 0.25$ (center), and $r/a = 0.3$ (right) for the case with Φ_1 . The upper figures correspond to the result evaluated with unsplit weights and the lower figures to the sum of the split weights. N is the toroidal symmetry number ($N = 10$ for LHD).

4.4 Case with Φ_1

Let us move on to the result of the case with Φ_1 . Figure 5 represents δn_C at $r/a = 0.2, 0.25$, and 0.3 , respectively. The upper figures are the results evaluated with the unsplit weight, w_C , and the lower figures with the sum of the split weights, $\sum_j w_{CC}^j$. As was for case without Φ_1 , the differences between the upper and lower results are in a tolerable level for the present analysis. The contributions of each driving force to the total density variation are shown in Fig. 6.

By comparing Fig. 5 with Fig. 3, we find that the phase structures are not largely changed. On the other hand, the amplitude of δn_C is increased by the inclusion of Φ_1 on all the surfaces. However, Fig. 6 indicates that the increase

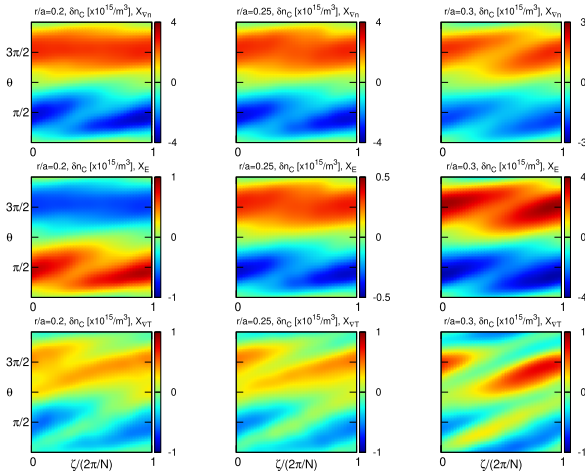


Fig. 6 Carbon density variation due to $X_{\nabla n}$ (top), X_E (center), and $X_{\nabla T}$ (bottom) for the case with Φ_1 . From left to right, each column corresponds to the flux surface at $r/a = 0.2$, $r/a = 0.25$, and $r/a = 0.3$, respectively. N is the toroidal symmetry number ($N = 10$ for LHD). Note that the color contour range is different for each plot.

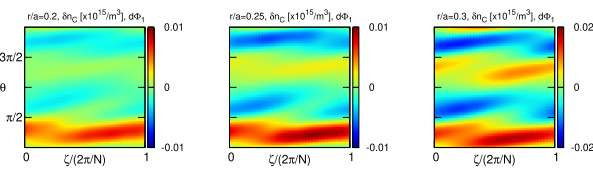


Fig. 7 Carbon density variation profile given by (32) on the flux surface at $r/a = 0.2$ (left), $r/a = 0.25$ (center), and $r/a = 0.3$ (right).

mainly results from the diffusion-related components, i.e., the $X_{\nabla n}$ and X_E components. At $r/a = 0.3$, the amplitude of the $X_{\nabla T}$ term, which involves Φ_1 in the microscopic flow as (13), is rather decreased by the inclusion of Φ_1 .

To examine the contribution of Φ_1 through (13), the density variation due to the relevant part of the term that includes Φ_1 in the flow

$$\begin{aligned} \delta n_C^{\Phi_1} &\equiv - \int dt \int d^3 v \mathbf{v}_d \cdot \nabla_r \frac{Z_C e \Phi_1}{T_i} f_{C0} \frac{\nabla T_i}{T_i} \\ &\simeq - \int dt \int d^3 v \mathbf{v}_m \cdot \nabla_r \frac{Z_C e \Phi_1}{T_i} f_{CM} \frac{\nabla T_i}{T_i}, \quad (32) \end{aligned}$$

is evaluated and shown in Fig. 7. The phase structure of $\delta n_C^{\Phi_1}$ is different from other terms, but its amplitude is too small to have an appreciable impact on the entire contribution of the $X_{\nabla T}$ component. Since the adiabatic response factor in the lowest order distribution function $\exp(-Z_C e \Phi_1 / T_i) \simeq 1 - Z_C e \Phi_1 / T_i$ contributes in a similar manner, this result indicates that Φ_1 affects the carbon density variation, and therefore the particle flux, mainly through the radial $E \times B$ drift, $\mathbf{v}_{E1} \cdot \nabla_r$, and its effects through the microscopic flow j_{a2} and the adiabatic response are insignificant. This fact may allow us to simplify the formulation to evaluate the impact of Φ_1 on the impurity transport.

5. Conclusion

In this article, we presented a new method to evaluate the impact of each driving force on neoclassical transport separately by a single Monte-Carlo δf simulation. As an application, we used the method to evaluate the relative impact of the driving forces on the impurity transport in an impurity hole plasma. In the application, we visually showed that the impact of the outward driving force of the ion temperature gradient can be as large as the impact of the inward driving force of the negative ambipolar E_r near the magnetic axis. We also showed that the contribution of Φ_1 in the drift-kinetic equation mainly results from the radial $E \times B$ drift, and the contributions through the microscopic energy flow and through the adiabatic response of the lowest order distribution function are relatively small.

As demonstrated by the application, this method can provide fruitful information on the causes of the density variations and which leads to our deeper understanding of the transport process. Unlike transport coefficients, the evaluation of the density variation in the two-dimensional form allows us to see the explicit configuration dependence of the transport. Although relatively insignificant in the present case, the spectrum components other than the $\sin \theta$ component become important in some cases. Our method can of course be used to study any Fourier components of δf_a within a reasonable range (in this study, we expanded δf_a as $\delta f_a = \sum_{m,n} [\tilde{f}_a^s \sin(m\theta - Nn\zeta) + \tilde{f}_a^c \cos(m\theta - Nn\zeta)]$ with the mode number ranges $-5 \leq m \leq 5$ and $0 \leq n \leq 5$). This aspect may be useful for comparative studies between different configurations of the device or between different devices.

The applicability of the method is wider than demonstrated above. First, as mentioned in the introduction, the impact of driving factors other than those considered in the example can be evaluated as well. Second, the method can be used to evaluate and visualize not only the spatial distribution but also the velocity distribution. This sort of application can be useful, for instance, to investigate the impacts of collisions and external heat sources. Third, the method can also be applied to evaluate the transport coefficients. This enables us to assess the global effects in terms of the transport coefficients by comparing them with those evaluated with local codes. The further applications enumerated here will be presented in future publications.

Acknowledgments

This work was performed under the auspices of the NIFS Collaborative Research Program, No. NIFS21KNST185, and also supported in part by JSPS KAKENHI Grant Number 21K03517. The simulations in this article were carried out on the Plasma Simulator at NIFS, Japan.

[1] J.M. García-Regaña *et al.*, Nucl. Fusion **57**(5), 056004 (2017).

- [2] A. Mollén *et al.*, Plasma Phys. Control. Fusion **60**, 084001 (2018).
- [3] J.L. Velasco *et al.*, Plasma Phys. Control. Fusion **60**, 074004 (2018).
- [4] K. Fujita *et al.*, J. Plasma Phys. **86**, 905860319 (2020).
- [5] K. Fujita *et al.*, Nucl. Fusion **61**, 086025 (2021).
- [6] M. Nunami *et al.*, Plasma Fusion Res. **12**, 1203039 (2017).
- [7] C.S. Chang and R.W. Harvey, Nucl. Fusion **23**(7), 935 (1983).
- [8] H. Yamaguchi and S. Murakami, Nucl. Fusion **58**(1), 016029 (2017).
- [9] Y. Idomura *et al.*, Phys. Plasmas **28**(1), 012501 (2021).
- [10] S. Sudo, Plasma Phys. Control. Fusion **58**(4), 043001 (2016).
- [11] S. Brunner *et al.*, Phys. Plasmas **6**, 4504 (1999).
- [12] W.X. Wang *et al.*, Plasma Phys. Control. Fusion **41**, 1091 (1999).
- [13] A.H. Boozer and G. Kuo-Petravic, Phys. Fluids **24**, 851 (1981).
- [14] S. Satake *et al.*, Comput. Phys. Commun. **255**, 107249 (2020).
- [15] K. Ida *et al.*, Phys. Plasmas **16**, 056111 (2009).
- [16] M. Yoshinuma *et al.*, Nucl. Fusion **49**, 062002 (2009).
- [17] D.R. Mikkelsen *et al.*, Phys. Plasmas **21**, 082302 (2014).
- [18] M. Nunami *et al.*, Phys. Plasmas **27**, 085501 (2020).
- [19] J.L. Velasco *et al.*, Nucl. Fusion **57**, 016016 (2017).
- [20] S. Satake *et al.*, Nucl. Fusion **45**, 1362 (2005).
- [21] S. Satake *et al.*, Comput. Phys. Commun. **181**, 1069 (2010).